metals

MDPI

Communication

A Comprehensive Study of Sn-Ga_2Te_3-SnTe Amorphous Alloys: Glass Formation and Crystallization Kinetics

Huan Zhang [1], Yaqi Zhang [1,2,*] and Gong Li [1,*]

[1] State Key Laboratory of Metastable Materials Science and Technology, College of Materials Science and Engineering, Yanshan University, Qinhuangdao 066004, China
[2] School of Mechanical and Electrical Engineering, Henan Institute of Science and Technology, Xinxiang 453003, China
* Correspondence: zhangyaqi_1988@163.com (Y.Z.); gongli@ysu.edu.cn (G.L.)

Abstract: In this paper, newly developed tellurium-based $[(Ga_2Te_3)_{34}(SnTe)_{66}]_{100-x}$-$Sn_x$ amorphous alloys were prepared by the melt-spun method, with a linear velocity of 40 m/s and injection pressure of 20 kPa under an Ar atmosphere. The glass-forming region was identified in the range of x = 0 to 10 mol%. The glass transition temperature T_g and crystallization onset temperature T_c decreased monotonically with the increasing Sn content in the whole compositional range, resulting in the decrease in the stability criterion ΔT from 33 K (S2) to 23 K (S10). The crystallization kinetics were systematically investigated based on the differential scanning calorimeter (DSC) under non-isothermal conditions. The activation energies of the S8 amorphous sample determined by Kissinger and Ozawa equations were E_g (201.1~209.6 kJ/mol), E_c (188.7~198.3 kJ/mol), E_{p1} (229.8~240.1 kJ/mol) and E_{p2} (264.2~272.6 kJ/mol), respectively. The microscopic structure of the S8 amorphous sample and its annealed glass-ceramics were also analyzed by X-ray diffraction (XRD), transmission electron microscopy (TEM) and selected-area electron diffraction (SAED). The crystalline products were identified as having a SnTe phase (primary crystalline phase) and Ga_6SnTe_{10} phase, thus providing a promising candidate for the development of high-performance thermoelectric glass-ceramic materials.

Keywords: amorphous materials; glass transition; crystallization kinetics; thermal stability; activation energy

check for updates

Citation: Zhang, H.; Zhang, Y.; Li, G. A Comprehensive Study of Sn-Ga_2Te_3-SnTe Amorphous Alloys: Glass Formation and Crystallization Kinetics. *Metals* **2023**, *13*, 532. https://doi.org/10.3390/met13030532

Academic Editor: Jordi Sort Viñas

Received: 2 February 2023
Revised: 2 March 2023
Accepted: 5 March 2023
Published: 6 March 2023

Copyright: © 2023 by the authors. Licensee MDPI, Basel, Switzerland. This article is an open access article distributed under the terms and conditions of the Creative Commons Attribution (CC BY) license (https://creativecommons.org/licenses/by/4.0/).

1. Introduction

Thermoelectric (TE) materials are capable of the conversion between electricity and thermal, rendering them desirable for waste heat recycling or power generation [1–3]. The TE efficiency was calculated by the equation $ZT = S^2\sigma T/\kappa$, where S is the Seebeck coefficient, σ is the electrical conductivity, κ is the total thermal conductivity, T is the absolute temperature and $S^2\sigma$ is defined as the power factor (PF) [4–6]. In recent years, the unique physical and electronic properties of tellurium and tellurium-based semiconductors have been harnessed to create high-efficiency thermoelectric generators due to their excellent comprehensive parameters (relatively high S, σ and low κ), when compared with insulators and metals [7]. Naturally, materials with intrinsic low thermal conductivity have been investigated as potential objectives with outstanding TE properties [8–10].

Chalcogenide amorphous materials, especially tellurium-based amorphous alloys, as the most conductive semiconductor amorphous materials, meanwhile, possess relatively low phonon energy and extremely low thermal conductivity, which also demonstrates their superior TE research prospects [11–16]. But, tellurium has a certain toxicity and inhalational exposure predominates, especially when absorbed through the skin. Typically, the manifestation of the acute toxicity of tellurium is nausea, vomiting and garlic odor on the breath [17,18]. Therefore, the operator should wear a self-priming filter dust mask, rubber gloves and safety protective clothing, preferably performing the actual experimental

operation in a vacuum glove box. However, the main obstacle hindering tellurium-based amorphous alloys for TE applications was their poor electrical conductivity.

In general, physical, chemical and mechanical properties are intimately related to micro-structure, such as atomic size, distribution and morphology [19–22]. Further investigations on glass-ceramics have illustrated that the properties of the amorphous matrix could be remarkably improved by controlling the partial crystallization [23–28]. Analogously, amorphous alloys with certain fractions of TE crystalline phases could promote the enhancement of the carrier concentrations and phonon scattering, thereby producing superior electrical transport properties while maintaining low thermal conductivity [29–33]. For instance, investigations of the Cu-As-Te amorphous system have verified this concept. The partial crystallization of the amorphous matrix lead to drastic increases in electrical conductivity by at least two orders of magnitude [30]. For the $Cu_{15}As_{30}Te_{55}$ amorphous composition, the electrical conductivity rose by about five orders of magnitude when the β-As_2Te_3 crystallization phase was presented in the amorphous matrix [31]. The Heusler glass-ceramics prepared by crystallizing the $NbCo_{1.1}Sn$ amorphous precursor at 893 K for 2 h exhibited a more enhanced electrical transport performance than the half-Heusler NbCoSn matrix from 310~710 K [32]. Compared to the $Fe_{78}Si_9B_{13}$ amorphous precursor, the *PF* for the $Fe_{78}Si_9B_{13}$ glass-ceramics annealed at 833 K for 20 min increased by 2200% at 575 K and increased by an average of about 1400% over the entire measurement temperature range [33].

Therefore, it is particularly essential to investigate the transition characteristics, crystallization kinetics parameters and precipitated phases in order to provide theoretical guidance for obtaining the desired properties and for the practical application of glass-ceramic materials. In this paper, newly developed tellurium-based $[(Ga_2Te_3)_{34}(SnTe)_{66}]_{100-x}$-$Sn_x$ amorphous alloys were fabricated using the melt-spun method and the glass-forming regions were ascertained. The glass transition behavior and crystallization process were then systematically investigated under non-isothermal conditions. Moreover, the characteristic temperatures and their associated activation energies were evaluated through the Kissinger and Ozawa methods on the basis of the differential scanning calorimeter (DSC). In addition, the microstructure evolutions were analyzed by X-ray diffraction (XRD), transmission electron microscope (TEM) and selected-area electron diffraction (SAED) and the crystalline products are also discussed.

2. Experimental

High-purity metals and compounds of Sn (99.99%), SnTe (99.9%) and Ga_2Te_3 (99.9%) were weighed on the stoichiometric ratio of $[(Ga_2Te_3)_{34}(SnTe)_{66}]_{100-x}$-$Sn_x$ (x = 0, 2, 4, 6, 8, 10 and 15, denoted as S0, S2, S4, S6, S8, S10 and S15, respectively). The mixtures were placed into a 12 mm inner diameter quartz tube with an oxygen–hydrogen flame under a vacuum of 10^{-3} Pa and then heated in a resistance furnace at 1153 K for 10 h. Throughout the isothermal heating period, the quartz tubes for each composition were rocked and turned upside down and the same processes were repeated at least five times to ensure a homogeneous mixture. The as-cast ingot was finally dropped below 303 K in the furnace and cut into small pieces for the melt-spun process. The as-cast ingot (8~10 g) was placed in a quartz tube and injected onto a high-speed rotating copper roller (20 kPa, 40 m/s, under an Ar atmosphere).

The grinding of the melt-spun flakes as powders was carried out for subsequent thermal and structural investigations. The thermodynamic characteristic temperature was determined by heating the powders (6~10 mg) in the Al pans from 300 K to 600 K at 20 K/min by DSC (Perkin-Elmer 8000). The non-isothermal crystallization kinetic parameters were analyzed by continuous heating at different heating rates (10, 20, 25 and 30 K/min). The structure characterizations of the melt-spun and annealed powders were measured by XRD (Rigaku Ltd., Tokyo, Japan, D/MAX/2500/PC, Cu K_α radiation with a wavelength of λ = 1.5406 Å) in the 2 θ range 20~60° at a speed of 2°/min. The melt-spun and annealed samples were first ground and polished on both sides until the thickness was

~30 μm and then were ultrasonically cleaned for 5 min in ethanol medium. The cleaned foils were pasted onto the copper grid and further thinned by the Gatan 695-B precision ion polishing system until electron transparency. The micro-structure was analyzed on the TEM (JEOL Ltd., Tokyo, Japan, JEM-2010) operated at 200 kV.

3. Results and Discussion

3.1. Structure Analysis and Glass Forming Region

The XRD patterns of the melt-spun $[(Ga_2Te_3)_{34}(SnTe)_{66}]_{100-x}$-$Sn_x$ samples are exhibited in Figure 1a. For the S0–S10 specimens, two widened peaks were detected in the diffraction patterns without any visible Bragg crystal peaks, confirming the completely amorphous structure. The micro-structure of the S8 sample was also characterized by TEM and SAED, as depicted in Figure 1b,c. A pure and homogeneous morphological surface can be observed in the S8 sample in the TEM image, as shown in Figure 1b, and the SAED pattern in Figure 1c was featured with a wide halo ring, which also demonstrated the amorphous nature of the S8 sample. For the S15 sample, four distinctive characteristic peaks were detected and identified as the SnTe crystalline phase (ICDD Xrd data: PDF#46-1210), indicating that the crystallization phenomenon began to occur. Therefore, the glass-forming region of the presently researched $[(Ga_2Te_3)_{34}(SnTe)_{66}]_{100-x}$-$Sn_x$ systems ranged from x = 0 to 10 mol% of Sn.

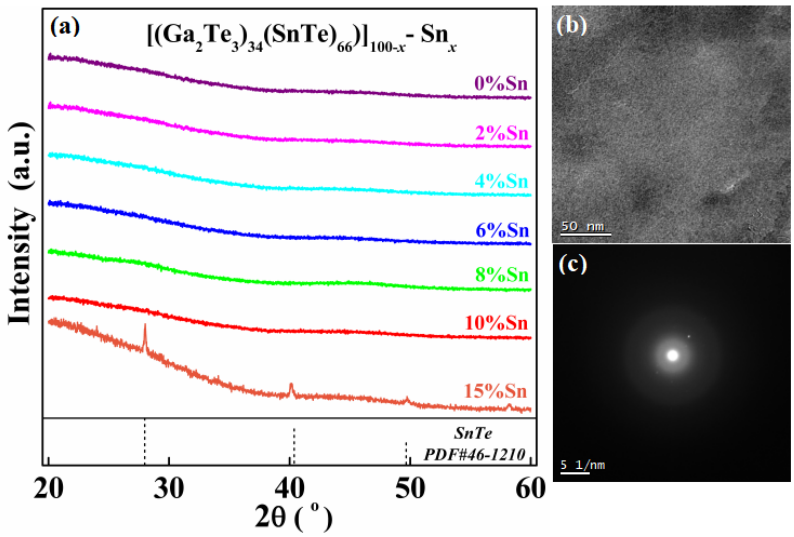


Figure 1. (**a**) XRD patterns of the melt-spun $[(Ga_2Te_3)_{34}(SnTe)_{66}]_{100-x}$-$Sn_x$ samples (x = 0, 2, 4, 6, 8, 10 and 15%), the TEM image (**b**) and corresponding SAED pattern (**c**) for S8 sample.

It should be noted that only a few Ge-Te or As-Te amorphous systems have been studied until now, such as the Cu-Ge-Te [34], Cu-As-Te [31], Cu-Ga-Te [35], Cu-Ge-As-Te [36] and Cu-As-Se-Te [13] systems. However, narrow-band-gap tellurium-based amorphous alloys, composed mainly of high-performance thermoelectric materials, such as SnTe, PbTe or Bi_2Te_3, have rarely been reported. In this work, the newly developed Ga_2Te_3-SnTe-Sn amorphous family provided a new option for thermoelectric materials and also broadened the research field of tellurium-based amorphous systems.

3.2. Thermal Analysis and Thermal Stability

The glass transition characteristics of $[(Ga_2Te_3)_{34}(SnTe)_{66}]_{100-x}$-$Sn_x$ completely amorphous samples ($x \leq 10\%$) were investigated by DSC and the heat flow traces with a fixed heating rate of 20 K/min were presented in Figure 2a. Three marked characteristic temperatures were clearly observed in the S2 cure: the glass transition temperature T_g, the crystallization onset temperature T_c and the crystallization peak temperature T_p, further confirmed the amorphous state of the investigated samples. As the Sn doping content

increased from 2 to 10, the crystallization behaviors underwent a transformation from a one-step reaction to a two-step reaction. The values of T_g, T_c, T_p and ΔT for the studied amorphous sample are listed in Table 1.

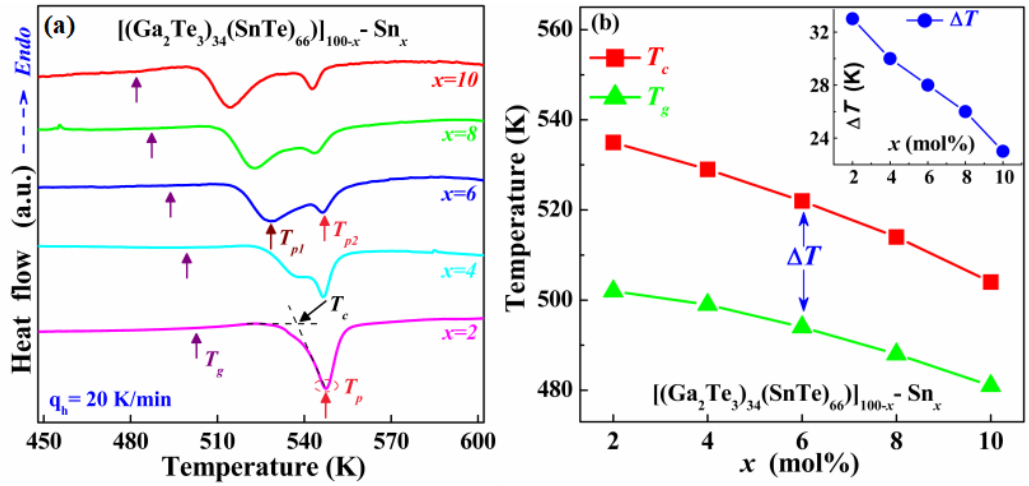


Figure 2. (**a**) Heat flow traces of the melt-spun $[(Ga_2Te_3)_{34}(SnTe)_{66}]_{100-x}$-$Sn_x$ samples (x = 2, 4, 6, 8 and 10%) and (**b**) composition dependence of the glass transition temperature T_g (Green triangle), the crystallization onset temperature T_c (Red square) and the supercooled liquid region ΔT (Blue circle).

Table 1. The characteristic temperatures T_g, T_c, T_{p1}, T_{p2} and ΔT for the $[(Ga_2Te_3)_{34}(SnTe)_{66}]_{100-x}$-$Sn_x$ amorphous samples (x = 2, 4, 6, 8 and 10).

Samples	Composition	T_g (K)	T_c (K)	T_{p1}(K)	T_{p2} (K)	ΔT (K)
S2	$[(Ga_2Te_3)_{34}(SnTe)_{66}]_{98}$-$Sn_2$	502	535	548	-	33
S4	$[(Ga_2Te_3)_{34}(SnTe)_{66}]_{96}$-$Sn_4$	499	529	537	547	30
S6	$[(Ga_2Te_3)_{34}(SnTe)_{66}]_{94}$-$Sn_6$	494	522	529	546	28
S8	$[(Ga_2Te_3)_{34}(SnTe)_{66}]_{92}$-$Sn_8$	488	514	525	545	26
S10	$[(Ga_2Te_3)_{34}(SnTe)_{66}]_{90}$-$Sn_{10}$	481	504	514	543	23

As depicted in Figure 2b, the T_g and T_c decreased monotonically with the increase in Sn content in the whole compositional range, which implies a weaker structural rigidity. The similar investigation results were also reported in both $Ag_x(Ge_5Sb_{25}Se_{70})_{1-x}$ and $Ag_{30+x}As_{28-x}Se_{21}Te_{21}$ glass systems, arising from the doped atoms, which could reduce the cross-linking degree of glass topological network [37,38]. The Dietzel stability criterion $\Delta T = T_c - T_g$ was widely adopted in order to analyze the thermal stability of amorphous alloys [39]. For all the studied samples, the values of ΔT were relatively low and decreased from 33 K (S2) to 23 K (S10). In particular, when the Sn content was higher than 10 mol%, owing to the excessive metallic features [40], the stability of the amorphous structure was destabilized and the crystalline phase began to precipitate, as observed in the XRD patterns of the S15 sample, which made it difficult to estimate its ΔT.

Although the doping of Sn reduced the T_g and ΔT of the Ga_2Te_3-SnTe-Sn amorphous system, it would provide a significant contribution to the strengthening of the conductivity of the amorphous materials. On this basis, the S8 amorphous alloy was selected as the subsequent target, on account of its excellent TE potential coupled with the relatively moderate thermal stability.

3.3. Non-Isothermal Crystallization Kinetics

The non-isothermal DSC traces of the S8 amorphous powers at different heating rates (10, 20, 25 and 30 K/min) are presented in Figure 3a.

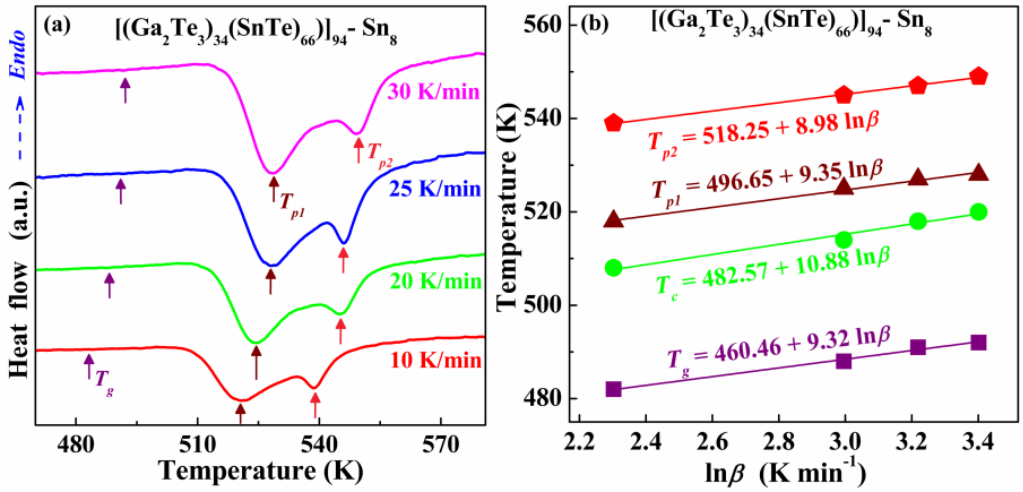


Figure 3. (**a**) Non-isothermal DSC curves at different heating rates (10, 20, 25 and 30 K/min) and (**b**) the relationship between characteristic temperatures T_g, T_c, T_{p1} and T_p versus ln(β) of the S8 amorphous samples.

All the DSC traces revealed an endothermic behavior of the vitrification from amorphous state to the under-cooled phase, followed by two separate exothermic peaks (named T_{p1} and T_{p2}, from low to high temperature, respectively), which correspond to the crystallization of the under-cooled liquid state. With the β increasing from 10 to 30 K/min, the characteristic temperatures moved to higher temperatures, revealing that the glass transition and crystallization processes were thermally activated. The values of T_g, T_c, T_{p1} and T_{p2} with different heating rates are listed in Table 2.

Table 2. The values of T_g, T_c, T_{p1}, T_{p2} and ΔT for S8 amorphous sample at different heating rates.

Heating Rate (K/min)	$[(Ga_2Te_3)_{34}(SnTe)_{66}]_{92}$-$Sn_8$				
	T_g (K)	T_c (K)	T_{p1} (K)	T_{p2} (K)	ΔT (K)
10	482	508	518	539	26
20	488	514	525	545	26
25	491	518	527	547	27
30	492	520	528	549	28

The sensitivity of the characteristic temperatures as a function of heating rate can be expressed by Lasocka's relations [41]:

$$T = A + B \ln \beta \quad (1)$$

where T is the characteristic temperature, A and B are constants, and the β stands for the heating rate. Figure 3b presents the relationships between T_g, T_c, T_{p1} and T_p versus the ln(β) of the S8 sample. The values of A and B were calculated by the linear fit. The larger the B value, the characteristic temperature was more sensitive to the heating rate. For the investigated S8 amorphous sample, both the glass transition and crystallization process exhibited clear kinetic influences and the B value for T_g (B_{Tg} = 9.32) were smaller than T_c (B_{Tc} = 10.88), implying that the crystallization behavior was more susceptible to the heating rate.

3.4. Activation Energy

The Kissinger method and the Ozawa equation are typically applied to evaluate the activation energy of the solid-state reactions under non-isothermal conditions and can be expressed as follows [42,43]:

Kissinger equation

$$ln\left[\frac{T^2}{\beta}\right] = \frac{E}{RT} + constant \quad (2)$$

Ozawa equation

$$\ln(\beta) = -\frac{E}{RT} + constant \quad (3)$$

where β represents the heating rate, R is the gas constant (8.314 J/mol K); T represents the characteristic temperature of T_g, T_c and T_p; and E denoted the apparent activation energy of the corresponding temperatures such as glass transformation activation energy (E_g) and the crystallization activation energy (E_c and E_p). Figure 4a,b, respectively, present the Kissinger and Ozawa plots of the S8 amorphous samples at different heating rates. The values of E were calculated by from the slopes of the linear by fitting the plots of the $\ln(T^2/\beta)$ versus $1000/T$ and $\ln(\beta)$ versus $1000/T$, and the corresponding E_g, E_c, E_{p1} and E_{p2} values are listed in Table 3.

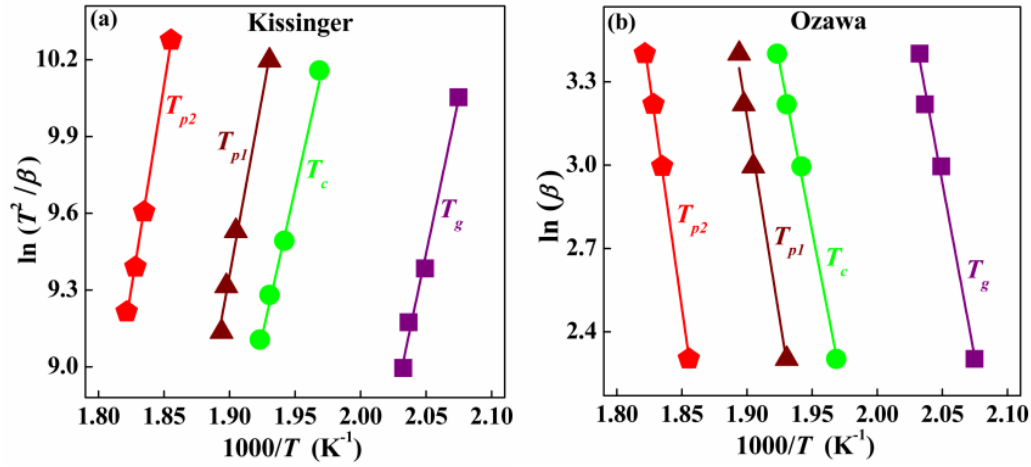


Figure 4. (**a**) Kissinger plots of $\ln(T^2/\beta)$ versus $1000/T$ and (**b**) Ozawa plots of $\ln(\beta)$ versus $1000/T$ for the S8 amorphous samples.

Table 3. The calculated apparent activation energy of the S8 amorphous samples by different methods.

	Activation Energy (kJ mol^{-1})			
Equation	E_g	E_c	E_{p1}	E_{pi}
Kissinger	201.1 ± 11.6	188.7 ± 10.7	229.8 ± 13.9	264.2 ± 7.3
Ozawa	209.6 ± 12.3	198.3 ± 6.9	240.1 ± 14.7	272.6 ± 7.1

The activation energies E determined by the Kissinger and Ozawa equations were fairly similar to each other, indicating that these methods were suitable for the investigated glasses and the results were highly reliable. Notably, for the S8 sample, the E_g (201.1 ± 11.6~209.6 ± 12.3 kJ/mol) > E_c (188.7 ± 10.7~198.3 ± 6.9 kJ/mol), implying that the energy barrier to be overcome for glass transition was lower than that for crystallization [44]. Furthermore, the $E_c < E_p$ demonstrated that the grain growth behavior was more difficult than the nucleation process under non-isothermal crystallization [45].

3.5. Crystallization Products

The XRD patterns of the S8 amorphous sample under different annealed temperatures are shown in Figure 5a. When the annealed temperature increased to 513 K (~T_c) for 5 min, four Bragg peaks near 2θ = 28.1°, 40.3°, 49.8° and 58.2° were imposed on the amorphous broad peaks, corresponding to the standard pattern of the SnTe crystalline phase, which was defined as the primary crystalline phase. As shown in Figure 5b, many small crystal

particles were clearly observed as precipitated and distributed in the sample. The SAED patterns presented amorphous rings and diffraction spots in Figure 5c, matching well with the crystalline SnTe phase, further confirming the coexistence of amorphous matrix and crystalline phase.

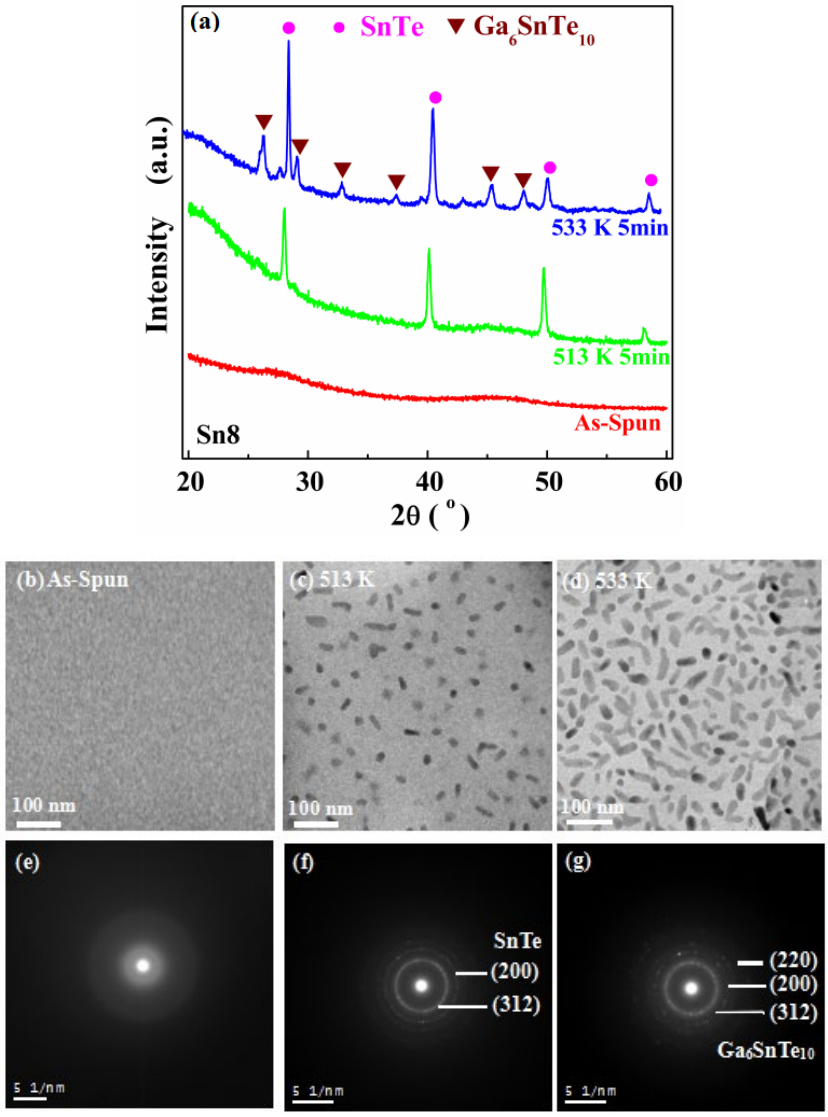


Figure 5. XRD patterns (**a**), the TEM image (**b**–**d**) and corresponding SAED pattern (**e**–**g**) of S8 amorphous sample under different annealed temperatures.

As the annealing temperature increased, more crystal diffraction peaks were detected precipitating from the amorphous background, and the intensity of the diffraction peaks increased significantly, indicating that the S8 sample was highly crystallized and the crystalline products were detected as the SnTe and Ga_6SnTe_{10} phases. When the annealed temperature increased to 533 K ($>T_{p1}$), rod-shaped and round particles with a size of approximately 100 nm were distributed in the matrix (Figure 5d). The SAED patterns (Figure 5g) presented bright and sharp diffraction rings and matched well with the polycrystalline SnTe and Ga_6SnTe_{10} phases, which were consistent with the XRD results of the annealed sample.

Recently, lead-free SnTe-based compounds were demonstrated to be promising TE materials due to their low toxicity and excellent electrical conductivity [46,47]. However, high thermal conductivity and low Seebeck coefficient devalue their TE application. Inversely, SnTe-based amorphous alloys exhibited extremely low thermal conductivity and high

Seebeck coefficients but poor electrical conductivity [12]. The SnTe-based glass-ceramics precipitated with the stable SnTe crystalline phase are thus anticipated to present a combination of low thermal conductivity, high Seebeck coefficient and moderate electrical conductivity, which would be beneficial in achieving the high-performance TE materials. Therefore, the S8 glass-ceramics might provide a reliable reference for the preparation of high-performance TE glass-ceramics materials.

4. Conclusions

The glass transition characteristics, crystallization kinetics and micro-structure evolutions of the newly developed $[(Ga_2Te_3)_{34}(SnTe)_{66}]_{100-x}$-$Sn_x$ tellurium-based alloys were systematically investigated in this paper.

The $[(Ga_2Te_3)_{34}(SnTe)_{66}]_{100-x}$-$Sn_x$ amorphous alloys were prepared using the melt-spun method, with a linear velocity of 40 m/s and injection pressure of 20 kPa under an Ar atmosphere.

The glass-forming region was identified in the range of x = 0 to 10 mol%.

T_g and T_c decreased monotonically with the increasing Sn content in the entire compositional range, resulting in the decrease in ΔT from 33 K (S2) to 23 K (S10).

For the S8 amorphous sample, the activation energies determined by the Kissinger and Ozawa equations were E_g (201.1~209.6 kJ/mol), E_c (188.7~198.3 kJ/mol), E_{p1} (229.8~240.1 kJ/mol) and E_{p2} (264.2~272.6 kJ/mol), respectively.

The crystalline products were identified as the SnTe phase (primary crystalline phase) and Ga_6SnTe_{10} phase, which are promising candidates for the development of high-performance TE glass-ceramic materials.

Author Contributions: H.Z.: Methodology, Investigation, Formal analysis, Writing-original draft. Y.Z.: Supervision, Data curation, Funding acquisition, Writing-review & editing. G.L.: Supervision, Funding acquisition, Writing-review & editing. All authors have read and agreed to the published version of the manuscript.

Funding: This work was supported by the open research fund of Songshan Lake Materials Laboratory (Grant No. 2022SLABFK01); the Natural Science Foundation of Henan Province (Grant No. 222300420161); the Province Science and Technology of Henan (Grant No. 202102310554) and the Postdoctoral Research Grant in Henan Province (Grant No. 202102081).

Data Availability Statement: Not applicable.

Conflicts of Interest: The authors declare that they have no known competing financial interests or personal relationships that could have appeared to influence the work reported in this paper.

References

1. Jiang, B.; Yu, Y.; Cui, J.; Liu, X.; Xie, L.; Liao, J.; Zhang, Q.; Huang, Y.; Ning, S.; Jia, B.; et al. High-Entropy-Stabilized Chalcogenides with High Thermoelectric Performance. *Science* **2021**, *371*, 830–834. [CrossRef] [PubMed]
2. Dong, W.; Zhou, Z.; Zhang, L.; Zhang, M.; Liaw, P.K.; Li, G.; Liu, R. Effects of Y, GdCu, and Al Addition on the Thermoelectric Behavior of CoCrFeNi High Entropy Alloys. *Metals* **2018**, *8*, 781. [CrossRef]
3. Qin, B.; Wang, D.; Liu, X.; Qin, Y.; Dong, J.-F.; Luo, J.; Li, J.-W.; Liu, W.; Tan, G.; Tang, X.; et al. Power Generation and Thermoelectric Cooling Enabled by Momentum and Energy Multiband Alignments. *Science* **2021**, *373*, 556–561. [CrossRef] [PubMed]
4. Zhang, Z.; Yan, Y.; Li, X.; Wang, X.; Li, J.; Chen, C.; Cao, F.; Sui, J.; Lin, X.; Liu, X.; et al. A Dual Role by Incorporation of Magnesium in YbZn2Sb2 Zintl Phase for Enhanced Thermoelectric Performance. *Adv. Energy Mater.* **2020**, *10*, 2001229. [CrossRef]
5. Poon, S.J. Recent Advances in Thermoelectric Performance of Half-Heusler Compounds. *Metals* **2018**, *8*, 989. [CrossRef]
6. Wu, Y.; Chen, Z.; Nan, P.; Xiong, F.; Lin, S.; Zhang, X.; Chen, Y.; Chen, L.; Ge, B.; Pei, Y. Lattice Strain Advances Thermoelectrics. *Joule* **2019**, *3*, 1276–1288. [CrossRef]
7. Yan, Q.; Kanatzidis, M.G. High-Performance Thermoelectrics and Challenges for Practical Devices. *Nat. Mater.* **2022**, *21*, 503–513. [CrossRef]
8. Aryana, K.; Stewart, D.A.; Gaskins, J.T.; Nag, J.; Read, J.C.; Olson, D.H.; Grobis, M.K.; Hopkins, P.E. Tuning Network Topology and Vibrational Mode Localization to Achieve Ultralow Thermal Conductivity in Amorphous Chalcogenides. *Nat. Commun.* **2021**, *12*, 2817. [CrossRef]

9. Hu, L.; Fang, Y.-W.; Qin, F.; Cao, X.; Zhao, X.; Luo, Y.; Repaka, D.V.M.; Luo, W.; Suwardi, A.; Soldi, T.; et al. High Thermoelectric Performance Enabled by Convergence of Nested Conduction Bands in Pb7Bi4Se13 with Low Thermal Conductivity. *Nat. Commun.* **2021**, *12*, 4793. [CrossRef]
10. Zhao, D.; Wang, L.; Wu, D.; Bo, L. Thermoelectric Properties of Cu2SnSe3-Based Composites Containing Melt-Spun Cu-Te. *Metals* **2019**, *9*, 971. [CrossRef]
11. Kang, S.; Fu, Y.; Gu, H.; Lin, C. Chalcogenide Glass for Thermoelectric Application. *J. Non-Cryst. Solids X* **2022**, *15*, 100111.
12. Zhang, H.; Zhang, Y.; Yu, P.; Wang, L.-M.; Li, G. Preparation and Thermoelectric Properties of Novel Tellurium-Based Glassy Semiconductors. *Scr. Mater.* **2021**, *203*, 114038. [CrossRef]
13. Lucas, P.; Conseil, C.; Yang, Z.; Hao, Q.; Cui, S.; Boussard-Pledel, C.; Bureau, B.; Gascoin, F.; Caillaud, C.; Gulbiten, O.; et al. Thermoelectric Bulk Glasses Based on the Cu-As-Te-Se system. *J. Mater. Chem. A* **2013**, *1*, 8917–8925. [CrossRef]
14. Vaney, J.-B.; Carreaud, J.; Morin, C.; Delaizir, G.; Piarristeguy, A.; Colas, M.; Cornette, J.; Le Parc, R.; Alleno, E.; Monnier, J.; et al. Thermoelectric Properties and Stability of Glasses in the Cu-As-Te System. *J. Am. Ceram. Soc.* **2017**, *100*, 2840–2851. [CrossRef]
15. He, S.; Li, Y.; Liu, L.; Jiang, Y.; Feng, J.; Zhu, W.; Zhang, J.; Dong, Z.; Deng, Y.; Luo, J.; et al. Semiconductor Glass with Superior Flexibility and High Room Temperature Thermoelectric Performance. *Sci. Adv.* **2020**, *6*, 8423–8431.
16. Alharbi, S.R.; Aly, K.A. Electrical and Thermoelectric Properties of Ternary Cu-Ge-Te Films. *J. Alloys Compd.* **2019**, *797*, 710–716. [CrossRef]
17. Ashraf, M.W.; Haider, S.I.; Solangi, A.R.; Memon, A.F. Toxicity of Tellurium and Its Compounds. *Phys. Sci. Rev.* **2022**, *5*, 112. [CrossRef]
18. Zare, B.; Nami, M.; Shahverdi, A.-R. Tracing Tellurium and Its Nanostructures in Biology. *Biol. Trace Elem. Res.* **2017**, *180*, 171–181. [CrossRef]
19. Zhao, W.; Li, G.; Wang, Y.Y.; Feng, S.D.; Qi, L.; Ma, M.Z.; Liu, R.P. Atomic Bond Proportions and Relations to Physical Properties in Metallic Glasses. *Mater. Des.* **2015**, *65*, 1048–1052. [CrossRef]
20. Ge, Y.; Cheng, J.; Yan, C.; Xue, L.; Zhang, B.; Liang, X. Devitrification and Sliding Wear Behaviors of AlFeSi Metallic Glass Coatings. *J. Mater. Res. Technol.* **2021**, *15*, 7022–7032. [CrossRef]
21. Chen, F.; Han, K.; Gao, M.; Zhang, Y.; Xu, W.; Huo, J.; Zhang, C.; Song, L.; Wang, J.-Q. Magnetocaloric Properties of Melt-Extracted Gd-Co-Al Amorphous/Crystalline Composite Fiber. *Metals* **2022**, *12*, 1367. [CrossRef]
22. Zhao, W.; Wang, Y.Y.; Liu, R.P.; Li, G. High Compressibility of Rare Earth-Based Bulk Metallic Glasses. *Appl. Phys. Lett.* **2013**, *102*, 031903. [CrossRef]
23. Hua, N.; Liao, Z.; Wang, Q.; Zhang, L.; Ye, Y.; Brechtl, J.; Liaw, P.K. Effects of Crystallization on Mechanical Behavior and Corrosion Performance of a Ductile Zr68Al8Ni8Cu16 Bulk Metallic Glass. *J. Non-Cryst. Solids* **2020**, *529*, 119782. [CrossRef]
24. Zhang, Q.; Liang, S.-X.; Jia, Z.; Zhang, W.; Wang, W.; Zhang, L.-C. Efficient Nanostructured Heterogeneous Catalysts by Electrochemical Etching of Partially Crystallized Fe-Based Metallic Glass Ribbons. *J. Mater. Sci. Technol.* **2021**, *61*, 159–168. [CrossRef]
25. Zhao, W.; Cheng, J.L.; Li, G. Quantitative Analysis of Structure Evolution of Zr-Cu Amorphous Alloys Caused by Cooling Rates Based on Atomic Bond Proportion. *Comput. Mater. Sci.* **2021**, *186*, 110011. [CrossRef]
26. Wang, C.; Yao, G.; Liu, J.; Mao, Y.; Leng, W.; Chen, Y.; Shen, X.; Wang, J.-Q.; Wang, R. Effects of Ca Doping on the Crystallization Kinetics of GeTe. *Appl. Phys. Lett.* **2021**, *118*, 211904. [CrossRef]
27. Zhao, J.; Gao, M.; Ma, M.; Cao, X.; He, Y.; Wang, W.; Luo, J. Influence of Annealing on the Tribological Properties of Zr-Based Bulk Metallic Glass. *J. Non-Cryst. Solids* **2018**, *481*, 94–97. [CrossRef]
28. Zhao, W.; Cheng, J.L.; Cheng, H.; Li, G. Effect of Low-Temperature Annealing on the Structure and Mechanical Properties of Zr-Cu Metallic Glasses. *Mater. Sci. Eng. A* **2016**, *673*, 239–242. [CrossRef]
29. Wang, G.; Zhang, Y.; Lotnyk, A.; Shi, H.; Chen, C. High Thermoelectric Performance in ZnSb-SnTe Pseudo-Binary Materials. *Scr. Mater.* **2021**, *194*, 113670. [CrossRef]
30. Vaney, J.-B.; Carreaud, J.; Piarristeguy, A.; Morin, C.; Delaizir, G.; Viennois, R.; Colas, M.; Cornette, J.; Alleno, E.; Monnier, J.; et al. Stabilization of Metastable Thermoelectric Crystalline Phases by Tuning the Glass Composition in the Cu-As-Te System. *Inorg. Chem.* **2018**, *57*, 754–767. [CrossRef]
31. Vaney, J.B.; Delaizir, G.; Alleno, E.; Rouleau, O.; Piarristeguy, A.; Monnier, J.; Godart, C.; Ribes, M.; Escalier, R.; Pradel, A.; et al. A Comprehensive Study of the Crystallization of Cu-As-Te glasses: Microstructure and thermoelectric properties. *J. Mater. Chem. A* **2013**, *1*, 8190–8200. [CrossRef]
32. Jung, C.; Dutta, B.; Dey, P.; Jeon, S.; Han, S.; Lee, H.-M.; Park, J.-S.; Yi, S.-H.; Choi, P.-P. Tailoring Nanostructured NbCoSn-Based Thermoelectric Materials via Crystallization of an Amorphous Precursor. *Nano Energy* **2021**, *80*, 105518. [CrossRef]
33. Yang, Z.; He, X.; Ning, Z.; Zhang, K.B.; Luo, F.; Li, C.C.; Ma, S.F.; Wei, P.; Zhao, W.Y.; Sun, Z.G.; et al. Effect of Nanocrystallization of Magnetic Amorphous Ribbon on Thermoelectric and Magnetic Properties. *J. Non-Cryst. Solids* **2020**, *535*, 119990. [CrossRef]
34. Gonçalves, A.P.; Lopes, E.B.; Rouleau, O.; Godart, C. Conducting Glasses as New Potential Thermoelectric Materials: The Cu-Ge-Te Case. *J. Mater. Chem.* **2010**, *20*, 1516–1521.
35. Gonçalves, A.P.; Lopes, E.B.; Delaizir, G.; Vaney, J.B.; Lenoir, B.; Piarristeguy, A.; Pradel, A.; Monnier, J.; Ochin, P.; Godart, C. Semiconducting Glasses: A New Class of Thermoelectric Materials? *J. Solid State Chem.* **2012**, *193*, 26–30.
36. Yang, Z.; Wilhelm, A.A.; Lucas, P. High-Conductivity Tellurium-Based Infrared Transmitting Glasses and Their Suitability for Bio-Optical Detection. *J. Am. Ceram. Soc.* **2010**, *93*, 1941–1944. [CrossRef]

37. Hu, H.; Zeng, H.; Li, L.; Wang, Y.; Guo, Y.; Jiang, Y.; Sun, L.; Chen, G. Crystallization Behaviors of Glasses in the (Ge5Sb25Se70)1−XAgx System. *Ceram. Int.* **2019**, *45*, 15073–15076. [CrossRef]
38. Zheng, J.; Li, L.; Yin, H.; Wang, Y.; Wei, J.; Zeng, H.; Xia, F. Guorong Chen Mutual Effects of Ag Doping and Non-Stoichiometric Glass Forming Units on the Structural, Thermal, and Electrical Properties of Ag30+xAs28−xSe21Te21 chalcogenide glasses. *Ceram. Int.* **2020**, *46*, 22826–22830. [CrossRef]
39. Zhang, Y.; Li, P.; Gao, P.; Tu, W.; Wang, L.-M. Non-Isothermal Crystallization Kinetics of Ga-Sn-Te Chalcogenide Glasses by Differential Scanning Calorimetry. *J. Mater. Sci.* **2017**, *52*, 2924–2933. [CrossRef]
40. Abd-Elrahman, M.I.; Hafiz, M.M.; Abdelraheem, A.M.; Abu-Sehly, A.A. Effect of Sn Additive on the Structure and Crystallization Kinetics in Ge-Se Alloy. *J. Alloys Compd.* **2016**, *675*, 1–7. [CrossRef]
41. Lasocka, M. The effect of scanning rate on glass transition temperature of splat-cooled Te85Ge15. *Mater. Sci. Eng.* **1975**, *23*, 173–177. [CrossRef]
42. Kissinger, H.E. Reaction kinetics in Differential thermal analysis. *Anal. Chem.* **1957**, *29*, 1702–1706. [CrossRef]
43. Ozawa, T. Kinetic analysis of derivative curves in thermal analysis. *J. Therm. Anal.* **1970**, *2*, 301–324. [CrossRef]
44. Ahmad, M.; Aly, K.A.; Dahshan, A.; Saddeek, Y.; Zakaly, H.M.H.; Elnaeim, A.M.A.; Ene, A. Physical Characterization and Crystallization Kinetics of Amorphous BiSe Chalcogenide Glasses. *J. Mater. Res. Technol.* **2022**, *16*, 1114–1121. [CrossRef]
45. Dong, Q.; Song, P.; Tan, J.; Qin, X.M.; Li, C.J.; Gao, P.; Feng, Z.X.; Calin, M.; Eckert, J. Non-Isothermal Crystallization Kinetics of a Fe-Cr-Mo-B-C Amorphous Powder. *J. Alloys Compd.* **2020**, *823*, 153783. [CrossRef]
46. Xu, X.; Cui, J.; Yu, Y.; Zhu, B.; Huang, Y.; Xie, L.; Wu, D.; He, J. Constructing van Der Waals Gaps in Cubic-Structured SnTe-Based Thermoelectric Materials. *Energy Environ. Sci.* **2020**, *13*, 5135–5142. [CrossRef]
47. An, D.; Wang, J.; Zhang, J.; Zhai, X.; Kang, Z.; Fan, W.; Yan, J.; Liu, Y.; Lu, L.; Jia, C.-L.; et al. Retarding Ostwald Ripening through Gibbs Adsorption and Interfacial Complexions Leads to High-Performance SnTe Thermoelectrics. *Energy Environ. Sci.* **2021**, *14*, 5469–5479. [CrossRef]

Disclaimer/Publisher's Note: The statements, opinions and data contained in all publications are solely those of the individual author(s) and contributor(s) and not of MDPI and/or the editor(s). MDPI and/or the editor(s) disclaim responsibility for any injury to people or property resulting from any ideas, methods, instructions or products referred to in the content.